Applied Geomatics (2024) 16:933–949
https://doi.org/10.1007/s12518-024-00593-4

ORIGINAL PAPER

Sensor fusion of robotic total station and inertial navigation system for 6DoF tracking applications

Tomas Thalmann[1] · **Hans Neuner**[1]

Received: 30 October 2023 / Accepted: 10 September 2024 / Published online: 28 September 2024

Abstract
This paper presents a novel approach for sensor fusion of robotic total station (RTS) and inertial navigation system (INS) to enable 6-degree-of-freedom (6DoF) pose estimation. Tight coupling of a spherical measurement model for RTS is developed, providing advantages over the traditional cartesian 3D-position measurement model, including supporting INS solution when distance measurements are unavailable and performing outlier detection in spherical observation space. Simulation studies demonstrate that replacing Global Navigation Satellite Systems (GNSS) with RTS for fusion with INS is beneficial in any environment (given line-of-sight (LOS) availability), even under ideal GNSS conditions. Furthermore, investigations on measurement models and failure identification over the entire range of RTS measurements reveal that the spherical model is advantageous over the cartesian model in certain regions. The developed methods are validated in a practical application for tilt compensation of an RTS pole, indicating a base 2D-RMSE of 3.8 mm for almost static and almost vertical poles, increasing with tilt and velocity.

Keywords Robotic total stations · Inertial navigation system · 6DoF pose estimation · Pole tilt compensation · Outlier detection

Introduction and related work

Six-degree-of-freedom (6DoF) estimation refers to the determination of 3D coordinates and 3D orientation of a rigid body in space. 6DoF pose estimation plays an important role in a variety of applications in engineering and manufacturing. On the one hand, position and orientation in space of an object or construction element is needed to enable or control further process steps. On the other hand, 6DoF estimation is often needed to transform measurements to a higher-level coordinate system, e.g., profile laser scanner data to a project coordinate system.

Examples in the field of industrial metrology (small-scale metrology, SSM) are probing devices (e.g., T-Probe or T-Scan) for laser trackers, which have been on the market for some time. These systems work by means of infrared LEDs on the probing device, whose 6DoF are evaluated by photogrammetric methods (Kyle and Loser 2003). At the other end of the accuracy spectrum are tilt compensators for GNSS poles (Luo et al. 2018). All types of mobile mapping systems (MMS) also fall into the same category. Currently, these mostly consist of GNSS/INS integration and rely on SLAM approaches in the absence of GNSS. Furthermore, there is a variety of GPS-related indoor positioning technologies based on UWB, Bluetooth or WLAN for 6DoF determination. However, these do not achieve the accuracy requirements for engineering and manufacturing. Vision-based systems are more interesting options between the accuracy classes of SSM (0.01 to 0.2 mm) and MMS based on GNSS or SLAM (1 to 10 cm) but have a limited working range and high installation costs. Very similar to these passive photogrammetric methods, light-based active systems from the gaming industry have also been investigated geodetically (Bauer et al. 2020). Approaches such as visual odometry (He et al. 2020) or laser-based SLAM approaches (Li et al. 2020) rely on environmental characteristics and exhibit dead-reckoning properties.

We see great potential in robotic total stations (RTSs) for 6DoF determination due to their flexible applicability (indoor

✉ Tomas Thalmann
tomas.thalmann@geo.tuwien.ac.at

Hans Neuner
hans.neuner@geo.tuwien.ac.at

[1] Department of Geodesy and Geoinformation, TU Wien, Wiedner Hauptstraße 8, Vienna 1040, Vienna, Austria

and outdoor), low calibration and infrastructure effort and high accuracy (1- 3 mm) and reliability. Pole tilt compensation for RTS (Maar 2022) has been analyzed by Eder (2022) in terms of efficiency and economy. They have also confirmed the additional uncertainty induced by tilt compensation stated by the manufacturer. The target application of the available solutions is limited to static point measurements. Additionally, for static point measurements a preliminary study on a probing device similar to the T-Probe for an RTS has been published by Schestauer et al. (2017).

While tilt compensation and probing devices improve efficiency and extend the possibilities, MMS based on RTS opens a new accuracy category. In the field of MMS, there have already been tests and preliminary investigations using a single RTS by Hesse and Vennegeerts (2014); Sternberg et al. (2013); Keller (2016); Linzer et al. (2019). Recently, Hesse et al. (2021) developed a vessel-based MMS utilizing both RTS and GNSS for the inspection of water and port infrastructure. Gao et al. (2017) pursued a different approach with the development of a pose measurement target sensor (PMTS) using a charge-coupled device (CCD) sensor. Whilst the accuracies are reported to be promising, the operating range is quite limited w.r.t. line-of-sight (LOS).

If the 6DoF pose of an object is of interest (e.g., a component such as railroad track, tunnel drilling machine or a retaining wall component), it can be derived from an MMS point cloud. Other solutions work by measuring at least 3 discrete points in the static case (see e.g., Zhou et al. 2022). Such measurement systems (e.g., rail measurement systems) use either 3 reflectors on the object with a static RTS or one RTS on the measurement trolley with at least 3 reference reflectors (Strübing 2015; Heunecke and Strübing 2018). These approaches only work in stop-and-go mode.

For kinematic 6DoF measurements, multiple target-tracking RTSs are used by Maxim et al. (2017) and Lerke and Schwieger (2021). The applications shown are the guidance of a UAV (Unmanned Aerial Vehicle) and localization of robots in building construction. The group of Vaidis et al. (2021, 2022) used a similar approach of an RTS network to measure highly accurate ground truth trajectories for a UGV (Unmanned Ground Vehicle). The drawbacks of these precise approaches are the costs (at least 3 RTS) and the (at least) 3 LOSs that must not be interrupted during the operation.

Our approach is to integrate the measurements of a single RTS with INS (inertial navigation system) measurements for a combined estimation of position and attitude of the target reflector. It can be used for any of the above mentioned applications and provides greater flexibility (compared to stop-and-go), operation range (compared to PMTS), and the possibility of a fully kinematic application with lower restrictions in terms of LOS interruption (compared to multi-RTS constellations).

In "Methodology", we describe the system and observation model of a tightly coupled integration as well as the test strategy for an RTS/INS integration. We then evaluate the model and investigate the achievable accuracy and the potential for improvement compared to GNSS/INS integration using thorough simulations (Section "Simulation Studies"). In "Smart pole experiments", we describe the developed prototype for tilt compensation of RTS poles as one usecase of our approach. We evaluate the achievable accuracy in the static and kinematic use cases using ground-truth reference points. A pole prototype was chosen for two reasons. On the one hand, both static and kinematic applications can be analyzed. On the other hand, a ground truth reference for the kinematic application can be realized by stabilized evaluation points, and additional uncertainties (e.g., detection of reference targets from laser scanning) are avoided. A summary and outlook can be found in the "Conclusion" section.

Methodology

In GNSS/INS integration, the well-known *navigation frame* (n-frame) is commonly used. It is defined as right-handed north-east-down (NED); the axes are leveled, north-aligned and attached to a vehicle (or moving object) frame (called the body frame, b-frame, denoted by superscript b).

In comparison, if the origin of the navigation frame is fixed to a certain point w.r.t. the earth, we denote this frame with superscript t (t-frame) and call it a *local geodetic frame*[1]. This frame is covered in the literature, e.g., Groves (2013, p. E-14ff), where the x-axis is aligned with the north direction and the z-axis points towards the down direction of the ellipsoid normal. The origin and orientation of this t-frame w.r.t. the earth-centered earth-fixed (ECEF) frame (superscript e, e-frame) are constant in time. INS integration and fusion algorithm are therefore similar to those for e-frame (commonly used for tight GNSS/INS integration).

The t-frame corresponds to a stationed/oriented RTS, in contrast, raw measurements of an RTS are related to a *local tangent-plane frame*. This l-frame, denoted by (superscript l), has a fixed origin w.r.t. the earth at the instruments zero point ($\boldsymbol{r}_o^e$). The z-axis coincides with the local gravity vector. The x-axis points towards the zero-position of the instruments horizontal angle sensor and does not necessarily correspond to a topographic direction (orientation unknown α_0). The y-axis completes the right-handed coordinate system. We introduce this new frame to represent raw RTS measurements

[1] Our naming convention may not seem intuitive, but the frame aligned with north is mostly named as *tangent-plane frame* and is denoted by (superscript t). To remain somewhat coherent with the literature, we also denote this frame by (^{t}), even though we consider *local geodetic frame* a more appropriate name for the aligned frame.

and decided to stick to a right-handed system in contrast to widespread left-handed systems in Geodesy because of interpretability of attitude representation. Both frames are shown in Fig. 1.

The relation between the l-frame and the e-frame is also constant in time and is comprised of two rotations $\boldsymbol{C}_e^t$ and $\boldsymbol{C}_t^l$. The first is defined by longitude and latitude of $\boldsymbol{r}_o^e$ and can be found e.g., in Groves (2013)[p. 76]. The latter describes a rotation by the orientation unknown α_0. Position $\boldsymbol{r}$, velocity $\boldsymbol{v}$, forces $\boldsymbol{f}$ and angular rates $\boldsymbol{\omega}$ can then be transformed by:

$$\begin{aligned} \boldsymbol{C}_t^l &= \begin{bmatrix} \cos(\alpha_o) & \sin(\alpha_o) & 0 \\ -\sin(\alpha_o) & \cos(\alpha_o) & 0 \\ 0 & 0 & 1 \end{bmatrix} \\ \boldsymbol{v}_{lb}^l &= \boldsymbol{C}_t^l\, \boldsymbol{C}_e^t\, \boldsymbol{v}_{eb}^e\,, \quad \boldsymbol{f}_{lb}^l = \boldsymbol{C}_t^l\, \boldsymbol{C}_e^t\, \boldsymbol{f}_{eb}^e \\ \boldsymbol{\omega}_{lb}^l &= \boldsymbol{C}_t^l\, \boldsymbol{C}_e^t\, \boldsymbol{\omega}_{eb}^e, \quad \boldsymbol{r}_{lb}^l = \boldsymbol{C}_t^l\, \boldsymbol{C}_e^t \left(\boldsymbol{r}_{eb}^e - \boldsymbol{r}_o^e\right) \end{aligned} \tag{1}$$

Strapdown and system model

As mentioned before, the introduced l-frame is earth-fixed, so derivation of the strapdown algorithm (SDA) and corresponding navigation equations is similar to the e-frame, widely used in GNSS/IMU integration (Titterton and Weston 2004, p. 126ff). Additionally, t-frame navigation equations have been presented in the literature, e.g., in Groves (2013, p. E-14ff). For the novel l-frame, we use identical time discrete navigation equations. The series expansion transitioning from continuous time to discrete time is limited to first-order terms:

$$\begin{aligned} \boldsymbol{C}_b^l(k+1) &\approx \boldsymbol{C}_b^l(k)\, \left[\boldsymbol{I}_3 + \boldsymbol{\Omega}_{ib}^b\, \tau\right] \\ \boldsymbol{f}_{ib}^l &= \frac{1}{2}\left[\boldsymbol{C}_b^l(k) + \boldsymbol{C}_b^l(k+1)\right]\, \boldsymbol{f}_{ib}^b \\ \boldsymbol{v}_{lb}^l(k+1) &\approx \boldsymbol{v}_{lb}^l(k) + \tau\, \left[\boldsymbol{f}_{ib}^l + \boldsymbol{g}_b^l\right] \\ \boldsymbol{r}_{lb}^l(k+1) &= \boldsymbol{r}_{lb}^l(k) + \left[\boldsymbol{v}_{lb}^l(k) + \boldsymbol{v}_{lb}^l(k+1)\right] \frac{\tau}{2} \end{aligned} \tag{2}$$

With the IMU sampling rate τ; $\boldsymbol{\omega}_{ib}^b$ and $\boldsymbol{f}_{ib}^b$ being the IMU angular rates and specific force measurements, matrix $\boldsymbol{\Omega}_{ib}^b$ is computed from angular rate vector $\boldsymbol{\omega}_{ib}^b$, building the skew-symmetric matrix $\boldsymbol{\Omega}_{ib}^b = \left[\boldsymbol{\omega}_{ib}^b\right]_\times$. Gravity $\boldsymbol{g}_b^l$ is the sum of centrifugal and gravitational accelerations and existing models for the e-frame (e.g., Groves 2013, p. 175) can be used by applying transformation (1).

In Eq. 2 correction terms such as earth rotation and Coriolis force are neglected. Because of the improved accuracy of RTS compared to GNSS, we analyzed the impact of these correction terms (approx. 5 mgon s^{-1} earth rotation and approx. 1.4 mm s^{-2} Coriolis force) on the basis of the industrial-grade MEMS IMU used in the following experiments. It turns out rules for GNSS/INS integration are also valid for RTS/INS, at least up to industrial-grade IMUs. Other effects arising from the definition of the l-frame (height and tilt error because of earth curvature) are also neglected in the current approach.

Sensor fusion in an INS is commonly performed using a closed loop Extended Kalman Filter (EKF) using error state formulation, see e.g., Jwo and Cho (2010). System and Measurement models are:

$$\begin{aligned} \delta\boldsymbol{x}_k &= \boldsymbol{T}_{k-1,k}\, \delta\boldsymbol{x}_{k-1} + \boldsymbol{w}_k \\ \delta z_k &= \boldsymbol{H}_k\, \delta\boldsymbol{x}_k + \boldsymbol{v}_k \end{aligned} \tag{3}$$

where $\delta\boldsymbol{x}_k \in \mathbb{R}^m$ describes the m-dimensional error state vector and the system noise is modeled as white noise sequences and follows a normal distribution $\boldsymbol{w}_k \sim \mathcal{N}\left(0, \boldsymbol{Q}_k\right)$. The n_k reduced measurements at epoch k are $\delta z_k \in \mathbb{R}^{n_k} = \boldsymbol{h}_k(\boldsymbol{x}_k^{SDA}) - z_k$ and measurement noise is $\boldsymbol{v}_k \sim \mathcal{N}(0, \boldsymbol{R}_k)$. The well-known prediction and update steps can be found in various publications, e.g., Grewal and Andrews (2014, p. 138), and an overview of the notation used in this work is given in Appendix A.

For a local-tangent-plane-frame implementation of an INS integration, the error state vector is defined as

$$\delta\boldsymbol{x}_{ins}^l = \left[\delta\boldsymbol{\psi}_{lb}^l\ \delta\boldsymbol{v}_{lb}^l\ \delta\boldsymbol{r}_{lb}^l\ \boldsymbol{b}_a\ \boldsymbol{b}_g\right]^T \quad , \tag{4}$$

where $\delta\boldsymbol{\psi}_{lb}^l$, $\delta\boldsymbol{v}_{lb}^l$, and $\delta\boldsymbol{r}_{lb}^l$ represent the errors in attitude (represented as Euler angles roll ϕ_{lb}^l, pitch θ_{lb}^l, yaw ψ_{lb}^l)), velocity and position. For some applications, it might be

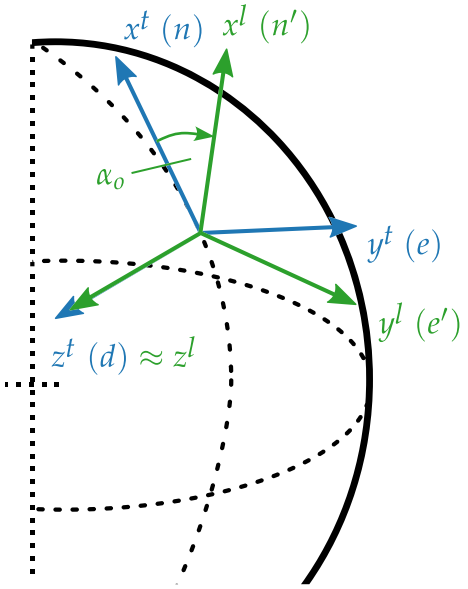

Fig. 1 Local tangent-plane frame (l-frame, green) and local geodetic frame (t-frame, blue) w.r.t. earth

worth thinking about a quaternion attitude representation to avoid Euler angle singularity. Additionally, inertial sensor biases $\boldsymbol{b}_a$ (accelerometers) and $\boldsymbol{b}_g$ (gyroscopes) are estimated because of turn-on biases. This gives an error state vector of 15 elements in total.

The derivation of the system model for a local frame is similar to that of the e-frame implementation since it is also earth fixed. The origin is transposed to a point usually on the surface, which is the RTS position in this paper. The frame is rotated by ellipsoidal latitude and longitude as described above. The system matrix may be written as (adopted from Groves 2013, p. 583):

$$\boldsymbol{F}_{ins}^{l} = \begin{bmatrix} \boldsymbol{0}_3 & \boldsymbol{0}_3 & \boldsymbol{0}_3 & \boldsymbol{0}_3 & \hat{\boldsymbol{C}}_b^l \\ \boldsymbol{F}_{21}^{l} & \boldsymbol{0}_3 & \boldsymbol{F}_{23}^{l} & \hat{\boldsymbol{C}}_b^l & \boldsymbol{0}_3 \\ \boldsymbol{0}_3 & \boldsymbol{I}_3 & \boldsymbol{0}_3 & \boldsymbol{0}_3 & \boldsymbol{0}_3 \\ \boldsymbol{0}_3 & \boldsymbol{0}_3 & \boldsymbol{0}_3 & \boldsymbol{0}_3 & \boldsymbol{0}_3 \\ \boldsymbol{0}_3 & \boldsymbol{0}_3 & \boldsymbol{0}_3 & \boldsymbol{0}_3 & \boldsymbol{0}_3 \end{bmatrix} \tag{5}$$

The submatrices are given by

$$\boldsymbol{F}_{21}^{l} = \left[-\hat{\boldsymbol{C}}_b^l \, \boldsymbol{f}_{ib}^{b}\right]_{\times} , \qquad \boldsymbol{F}_{23}^{l} = \boldsymbol{C}_e^l \, \delta \boldsymbol{g}_b^e \, \boldsymbol{C}_l^e \, . \tag{6}$$

Note that $\hat{\boldsymbol{C}}_e^l$ is constant because both frames are earth fixed and $\hat{\boldsymbol{C}}_b^l$ is the rotation matrix representation of attitude derived from Euler angles $\boldsymbol{\psi}_{lb}$. The gravity error w.r.t. e-frame $\delta \boldsymbol{g}_b^e$ can be found in existing GNSS/IMU literature, e.g., Groves (2013, p. 583).

The transition matrix $\boldsymbol{T}_{k-1,k}$ follows from the system matrix solving the differential equation by using the power series expansion of the matrix exponential function again limited to first order:

$$\boldsymbol{T}_{k-1,k} = \exp\left(\boldsymbol{F}_{ins} \, \tau_p\right) \approx \boldsymbol{I} + \boldsymbol{F}_{ins}^{l} \, \tau_p \, , \tag{7}$$

which allows the prediction of the system state from epoch t_{k-1} to epoch t_k with $\tau_p = t_k - t_{k-1}$ being the prediction interval, usually identical to the IMU sampling rate τ. Since RTS measurements do not show a constant measurement rate, the prediction interval τ_p must be adjusted in epochs of measurements to fit the timestamp of measurement.

Measurement models

For the local tangent-plane l-frame EKF, the positions of the IMU $(_b)$ are estimated as right-handed coordinate tuple consisting of pseudo-north, -east and -down $\boldsymbol{r}_{lb}^{l} = \left[x_{lb}^{l} \; y_{lb}^{l} \; z_{lb}^{l}\right]^T$. On the other hand, measurements of a RTS include the unoriented horizontal direction (angle between instruments zero-direction and target) R_{la}^{l}, vertical angle (angle between zenith and target) ζ_{la}^{l} and slope distance D_{la}^{l}, composing the spherical measurement vector of the prism position $(_a)$ w.r.t. to the l-frame.

$$\boldsymbol{p}_{la}^{l} = \begin{bmatrix} R_{la}^{l} \\ \zeta_{la}^{l} \\ D_{la}^{l} \end{bmatrix} . \tag{8}$$

Note that orientation unknown α_0 does not need to be considered within the l-frame since it is already modeled through the relation between the t- and l-frame.

In terms of measurement models for RTSs, two possible approaches exist. First, spherical raw observations $\boldsymbol{p}_{la}^{l}$ are converted to cartesian prism positions ${}^{o}\boldsymbol{r}_{la}^{l}$ with corresponding propagated variance-covariance-matrix (VCM) $\boldsymbol{\Sigma}_r$ outside of the EKF. We call this approach *Cartesian Updates*. Second, the spherical observations are directly input to the filter (*Spherical Updates*).

Cartesian measurement model

Considering the leverarm $\boldsymbol{l}_{ba}^{b}$ describing the displacement of the measured prism position a and the origin of the body frame b, the cartesian measurement model reads:

$$\delta z_k^r = {}^{o}\boldsymbol{r}_{la}^{l} - \left(\hat{\boldsymbol{r}}_{lb}^{l} + \hat{\boldsymbol{C}}_b^l \, \boldsymbol{l}_{ba}^{b}\right) . \tag{9}$$

The measurement matrix $\boldsymbol{H}_k$ is given by Groves (2013) [p. 599]:

$$\boldsymbol{H}_k^r = \left[\boldsymbol{H}_{r1} \; \boldsymbol{0}_3 \; -\boldsymbol{I}_3 \; \boldsymbol{0}_3 \; \boldsymbol{0}_3\right] , \tag{10}$$

where $\boldsymbol{H}_{r1} \approx \left[\hat{\boldsymbol{C}}_b^l \, \boldsymbol{l}_{ba}^{b}\right]_{\times}$.

Since GNSS receivers usually provide velocity measurements by means of Doppler measurements, which are also used in the GNSS reference solution in "Comparison of RTS and GNSS" section, the corresponding velocity parts of the measurement models are given as follows:

$$\begin{aligned} \delta z_k^v &= {}^{o}\boldsymbol{v}_{la}^{l} - \left(\hat{\boldsymbol{v}}_{lb}^{l} + \hat{\boldsymbol{C}}_b^l \left(\hat{\boldsymbol{\omega}}_{ib}^{b} \times \boldsymbol{l}_{ba}^{b}\right)\right) \\ \boldsymbol{H}_k^v &= \left[\boldsymbol{H}_{v1} \; -\boldsymbol{I}_3 \; \boldsymbol{0}_3 \; \boldsymbol{0}_3 \; \boldsymbol{H}_{v5}\right] \\ \boldsymbol{H}_{v1} &\approx \left[\hat{\boldsymbol{C}}_b^l \left(\hat{\boldsymbol{\omega}}_{ib}^{b} \times \boldsymbol{l}_{ba}^{b}\right)\right]_{\times} \\ \boldsymbol{H}_{v5} &\approx \hat{\boldsymbol{C}}_b^l \left[\boldsymbol{l}_{ba}^{b}\right]_{\times} \end{aligned} \tag{11}$$

giving the GNSS measurement model:

$$\delta z_k = \begin{bmatrix} \delta z_k^r \\ \delta z_k^v \end{bmatrix} \qquad \boldsymbol{H}_k = \begin{bmatrix} \boldsymbol{H}_k^r \\ \boldsymbol{H}_k^v \end{bmatrix} \tag{12}$$

Spherical measurement model

The relation between the spherical measurements $\boldsymbol{p}_{la}^{l}$ and cartesian positions $\boldsymbol{r}_{la}^{l}$ is given by

$$\boldsymbol{r}_{la}^{l} = \begin{bmatrix} D_{la}^{l} \sin\zeta_{la}^{l} \cos R_{la}^{l} \\ D_{la}^{l} \sin\zeta_{la}^{l} \sin R_{la}^{l} \\ -D_{la}^{l} \cos\zeta_{la}^{l} \end{bmatrix} - : \boldsymbol{\Xi}^{-1}\left(\boldsymbol{p}_{la}^{l}\right) , \tag{13}$$

assuming that the origin of both (spherical and cartesian) systems coincide and describe the origin of the l-frame, which is equal to the reference point of the RTS. The inverse task is computed by

$$\boldsymbol{p}_{la}^{l} = \begin{bmatrix} \arctan\left(y_{la}^{l}/x_{la}^{l}\right) \\ \arccos\left(-z_{la}^{l}/\sqrt{{x_{la}^{l}}^{2}+{y_{la}^{l}}^{2}+{z_{la}^{l}}^{2}}\right) \\ \sqrt{{x_{la}^{l}}^{2}+{y_{la}^{l}}^{2}+{z_{la}^{l}}^{2}} \end{bmatrix} =: \boldsymbol{\Xi}\left(\boldsymbol{r}_{la}^{l}\right) . \tag{14}$$

Then (9) changes to

$$\delta z_k^p = \begin{bmatrix} {}^{o}R \\ {}^{o}\zeta \\ {}^{o}D \end{bmatrix} - \boldsymbol{\Xi}\left(\hat{\boldsymbol{r}}_{lb}^{l} + \hat{\boldsymbol{C}}_{b}^{l}\boldsymbol{l}_{ba}^{b}\right) . \tag{15}$$

The observation matrix $\boldsymbol{H}_k^p$ is given by

$$\boldsymbol{H}_k^p = \begin{bmatrix} \boldsymbol{H}_{p1} \; \boldsymbol{0}_3 \; \boldsymbol{H}_{p3} \; \boldsymbol{0}_3 \; \boldsymbol{0}_3 \end{bmatrix} \tag{16}$$

where the submatrices are derived by symbolic computation and automatic differentiation:

$$\begin{aligned} \boldsymbol{H}_{p1} &= -\frac{\partial \boldsymbol{\Xi}\left(\hat{\boldsymbol{r}}_{lb}^{l} + \hat{\boldsymbol{C}}_{b}^{l}\boldsymbol{l}_{ba}^{b}\right)}{\partial \boldsymbol{\psi}_{lb}} \\ \boldsymbol{H}_{p3} &= -\frac{\partial \boldsymbol{\Xi}\left(\hat{\boldsymbol{r}}_{lb}^{l} + \hat{\boldsymbol{C}}_{b}^{l}\boldsymbol{l}_{ba}^{b}\right)}{\partial \boldsymbol{r}_{lb}} \end{aligned} \tag{17}$$

This spherical measurement model has two important advantages over the cartesian measurement model:

1. In cases where no distance measurements are carried out by the instruments, angle information can still be used to support the INS strapdown solution.
2. Outlier detection can be performed within the EKF at originating spherical observation space.

On the other hand this model has two drawbacks:

1. Computationally the spherical model is much more expensive.
2. The cartesian model (10) is supposed to have less nonlinearities than the spherical model (16).

Considering the fact that post-processing is used in our current implementation, computational complexity should not be an issue w.r.t. modern day computing resources. Concerning nonlinearities the necessity of negligible linearization errors in both the system and observation models for EKFs can be upheld for the spherical model, as show by investigations conducted during this research.

Testing strategy

The implemented testing strategy consists of the well-known local overall model test statistic (LOM) based on the KF innovations, see Teunissen (1998) (for details of the used notation, see Appendix A):

$$T_{LOM,k} = \boldsymbol{d}_k^T \boldsymbol{D}_k^{-1} \boldsymbol{d}_k \quad \text{with} \quad T_{LOM,k} > \chi^2_{1-\alpha,n_k} \tag{18}$$

If a model error is indicated by the LOM statistic, further investigations are performed. This can be done using the mean shift model, which allows a general approach to test for q outliers described in Appendix B.

Individual measurement

The test for inconsistency in individual measurement can be derived by choosing $\boldsymbol{E} = \boldsymbol{\eta}_i$ (the i-th unit vector) with $q = 1$. Alternative hypothesis, test statistic and rejection criterion for the i-th measurement of epoch k are Wieser et al. (2004):

$$\begin{aligned} H_{a,i,k} &: E\{\delta z_k\} = \boldsymbol{H}_k \delta \boldsymbol{x}_k + \boldsymbol{\eta}_i \Delta \\ t_{i,k} &= \frac{\boldsymbol{\eta}_i^T \boldsymbol{D}_k^{-1} \boldsymbol{d}_k}{\sqrt{\boldsymbol{\eta}_i^T \boldsymbol{D}_k^{-1} \boldsymbol{\eta}_i}} \\ |t_{i,k}| &> z_{1-\alpha_{q=1}/2} \end{aligned} \tag{19}$$

For example, with $\boldsymbol{E} = \boldsymbol{\eta}_3 = \begin{bmatrix} 0 \; 0 \; 1 \end{bmatrix}^T$, we are able to test for an error in the distance measurement ($\Delta = \Delta_D$) in the spherical measurement model (15) or for a z-coordinate error ($\Delta = \Delta_z$) in the cartesian measurement model (9).

Assuming that an outlier is primarily occurring at distance measurements, there are two approaches to handle such an outlier for the cartesian model. If the prism is close to one of the planes spanned by two coordinate axes, one could test against a failure in two components at a time, e.g., the x- and y-components for a vertical angle ζ of approximately 100 gon. The other approach is to model a distance outlier for cartesian measurement equations. Both are shown in Appendix B. The first approach is less efficient in terms of detectability, and the second approach is identical to the

spherical measurement model, but both approaches lack the possibility for proper bias elimination.

Harmonizing error probabilities

In such a testing strategy, it is useful to harmonize the error probabilities of detection (LOM) and identification (19). This leads to two relations that define error probability α, power of the test $1-\beta$, error probability of individual test α_q and the number of measurements n_k w.r.t. each other Baarda (1968):

$$\begin{aligned} \chi^2_{1-\alpha_q,q} &= \chi^2_{\beta,q,\lambda} \\ \chi^2_{1-\alpha,n_k} &= \chi^2_{\beta,n_k\lambda} \end{aligned} \tag{20}$$

For both our measurement models, we choose a type 2 error probability of $\beta = \beta_q = 20\%$ and a type 1 error probability of an individual test $\alpha_{q=1} = 0.2\%$. The number of measurements $n_k = 3$ for both models.

This gives a type 1 error probability for the LOM of $\alpha = 1.0\%$ and a type 1 error probability of $\alpha_{q=2} = 0.5\%$ for the group test described in Eq. B12.

Simulation studies

The formulated methodology and its implementation in Python are evaluated in several simulations. Using these simulations two research questions are addressed:

- Is it advantageous, and if so, how large is the benefit of replacing GNSS with RTS for fusion with INS? As mentioned in the introduction, RTSs have the obvious advantage of being independent of satellite visibility or sky obstruction. Additionally, independence from electrical installations (power lines or transformers) and reflective surfaces (multipath). But how does this comparison turn out in a *GNSS-ideal* environment?
- What is the benefit of using the novel spherical measurement model instead of cartesian updates?

The following simulations are based on an initialization routine, designed as an eight-shaped movement of the prism, while holding the pole tip attached to a fixed ground point. The trajectory is shown in Fig. 2 (right). The positions are generated by pole tilts of up to 35 gon (roll) and up to 25 gon (pitch). The RTS is located at (0.0, 0.0, 0.0), and the ground point is at (20.0, 7.5, 1.8). The simulated pole height is 1.4 m and all scenarios assume a correctly known mounting vector from the IMU to the prism (and GNSS reference point respectively) of $\boldsymbol{l}^b_{ba} = \left[\,-0.002\;-0.012\;-0.238\right]$ m. Such a simulation scenario represents the application range of the proposed prototype for large scale metrology.

The simulated scenario of 30 s duration includes 2 phases of initialization routines, as shown in Fig. 2 (left):

- from second 4 to 12 with two eight-shapes with the IMU pointing in direction of LOS
- from second 17 to 25 with two eight-shapes with the IMU pointing perpendicular to LOS

The design was developed and chosen from both the authors' personal simulation runs and the work and findings of Teodori and Neuner (2021). Key aspects to consider are horizontal acceleration changes that are crucial for the observability of the yaw error state and the anisotropy of RTS measurement accuracy (along and perpendicular to LOS).

The stochastic model of the simulated IMU is comprised of the sensor white noise and bias instability, both of which are defined by their corresponding power spectral densities (PSDs), as shown in Table 1. The values are taken from long-term evaluation experiments of the IMU used in the experiments.

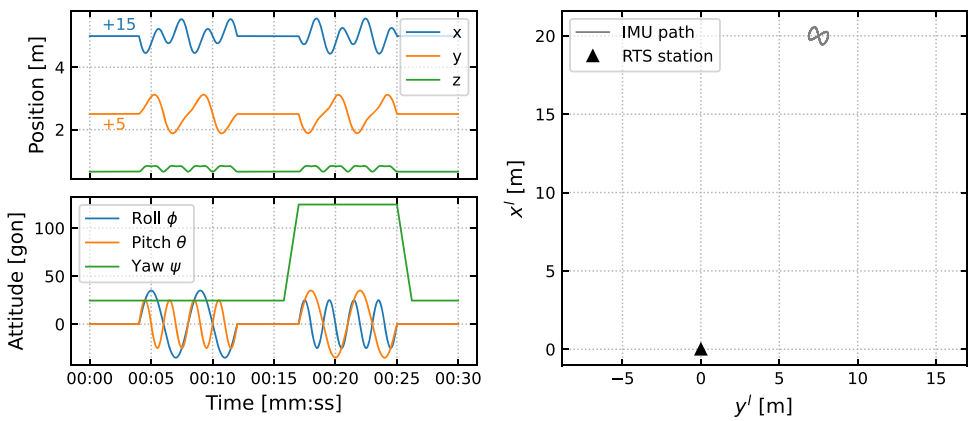

Fig. 2 **(left)** Simulated profiles for IMU position and attitude. **(right)** Simulated IMU trajectory in l-frame w.r.t. the RTS station

Table 1 IMU Simulation parameters

Parameter	Notation	Value
Accelerometer white noise	$\sqrt{S_a}$	$160\mu g/\sqrt{\text{Hz}}$
Gyro white noise	$\sqrt{S_g}$	$1 \times 10^{-2}\text{deg/s}/\sqrt{\text{Hz}}$
Accelerometer bias instability	$\sqrt{S_{ba}}$	$1.5 \times 10^{-4}\text{m/s}^2$
Gyro bias instability	$\sqrt{S_{bg}}$	$2.5 \times 10^{-3}\text{deg/s}$

Comparison of RTS and GNSS

The GNSS observations are simulated according to the following exemplary stochastic model, derived from Luo et al. (2018) with a measurement frequency of 20 Hz:

$$\begin{aligned}\boldsymbol{\Sigma}_{GNSS,pos} &= \begin{pmatrix} 0.6^2 & 0.17^2 & 0.12^2 \\ 0.17^2 & 0.5^2 & -(0.25^2) \\ 0.12^2 & -(0.25^2) & 0.8^2 \end{pmatrix} \text{[cm]}^2 \,, \\ \boldsymbol{\Sigma}_{GNSS,vel} &= \begin{pmatrix} 5.7^2 & 1.3^2 & 1.9^2 \\ 1.3^2 & 4.8^2 & -(2.0^2) \\ 1.9^2 & -(2.0^2) & 6.8^2 \end{pmatrix} \text{[cm/s]}^2 \,. \end{aligned} \tag{21}$$

This stochastic model is derived from a high-end handheld professional GNSS pole and is supposed to represent the best solutions in terms of accuracy on the market. For consumer-grade GNSS antennas and receivers on UAV or UGV mounted MMS, the comparison is accordingly different.

The RTS observations are simulated with a measurement frequency of 7.5 Hz and $\sigma_D = 3$ mm, $\sigma_{R,\zeta} = 0.3$ mgon, $\sigma_{ATR} = 1.8$ mm according to Leica Geosystems (2016) (ATR, Automatic Target Recognition, as the dominant source of measurement uncertainty at close ranges). The small deviations from the manufacturer's (static) specifications result from the findings of Thalmann and Neuner (2021) in a kinematic experiment setup. Again it is worth mentioning that some RTS achieve measurement rates of up to 20 Hz as well.

Figure 3 shows the estimated posterior position standard deviations of a GNSS/INS (orange) and an RTS/INS (blue) filter compared to their simulated values from 1000 Monte-Carlo-Simulation (MCS) runs ($\tilde{\sigma}$ plotted as gray areas). We can deduce that the filter implementation is correct in terms of posterior standard deviation (SD) estimation by comparing gray areas (MCS) and corresponding estimated values of the filter. Furthermore, we conclude the unbiasedness of the EKF estimator implementation by analyzing the residuals w.r.t. to ground truth.

From Fig. 3, we can also deduce the improvement in position estimates by replacing GNSS with one RTS. This heavily depends on the position of the prism w.r.t. the RTS and the orientation unknown α_0 because of horizontal anisotropy of measurement accuracy both for GNSS and RTS.

To obtain a better understanding of the change in accuracy, we analyzed the simulations results for $R \in [0, ..., 100]$ gon and $\alpha_0 \in [0, ..., 100]$ gon. Subsequently, the median improvement and the improvement range (defined by minimal and maximal improvement) are computed over all possible setups (=combinations R and α_0). Here, improvement is defined as $(\sigma_{GNSS} - \sigma_{RTS})/\sigma_{GNSS}$. The results for nearly horizontal LOSs (the case for the following application of pole tilt compensation) are shown in Fig. 4.

Overall, comparing RTS/INS and GNSS/INS fusion, every state parameter improves when utilizing an RTS. The z-components are not affected by anisotropy, so the improvement is constant across all setups. For attitude parameters, the improvement relative to GNSS is 10 to 22 %. The largest benefit can be found at the estimated yaw accuracy because roll and pitch angles are already well determined by sensing gravity. In terms of position estimation, shown in Fig. 4(b), the largest improvement of approximately 55 % is found in the z-component. On the one hand, this component is weakly determined with GNSS, and on the other hand, the distance accuracy of the RTS has the smallest influence on z. Depending on the RTS setup the improvement of the horizontal

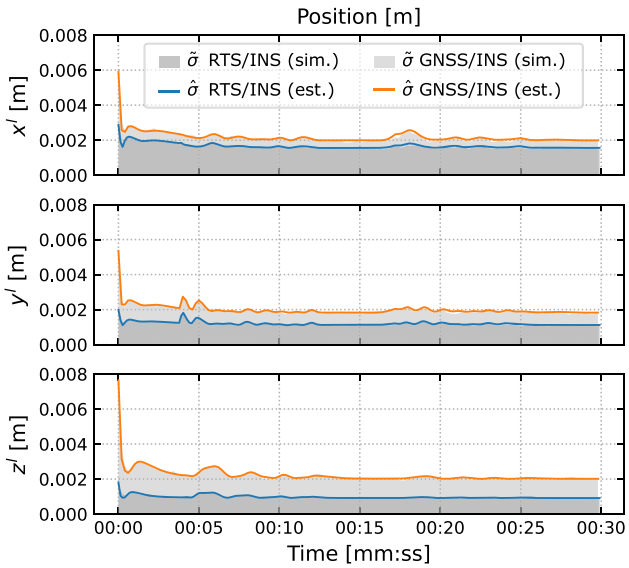

Fig. 3 Post-update stochastics for position of GNSS/INS and RTS/INS integration in comparison. Gray areas visualize empirical SDs from MCS, whereas the colored lines are the estimated SDs from EKF

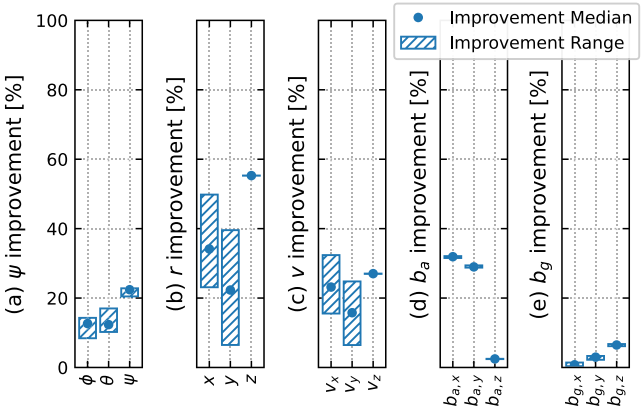

Fig. 4 Accuracy improvement of RTS/INS compared to GNSS/INS solution immediately after initialization routine finished (at timestamp 00:28)

components strongly varies between 50 and 7 %. Since the north (x) component is worse determined than the east (y) component using GNSS (cf. Santerre 1991) the improvement by using RTS is larger. The range of improvements is related to the direction of the LOS, e.g., if the RTS distance D is measured in direction of east we have the smallest improvement in the east component and the largest improvement in the north component. Despite the lack of direct observations of velocities, an increase in accuracy for velocities can be achieved with RTS, see Fig. 4(c). The estimation of accelerometer biases of x and y (mostly nearly horizontally aligned) can be improved by about 30 % whereas the z-component is already well determined using GNSS, see Fig. 4(d) . The gyro biases Fig. 4(e) improvements are close to zero or negligible.

To conclude, a replacement of GNSS by RTS is beneficial in any case despite the missing velocity observations (and therefore reduced number of observations) and the lower measurement rate (approx. 7.5 Hz compared to 20 Hz). The improved position accuracy of RTS also compensates for the missing coupling of attitude errors with velocity errors (cf. Teodori and Neuner 2021).

Measurement models and testing

To investigate the differences between the cartesian and spherical measurement models two scenarios are considered during simulation studies:

1. Time periods in which outliers occur in the distance measurement (Δ_D). These are highlighted as gray areas in Fig. 5. As a quantity for this outlier, we use the parameter of statistical reliability, the minimum detectable bias (MDB). For the distance measurement within the spherical measurement model the MDB $\nabla_D = 14.3$ mm, which is approximately $4.8 \times \sigma_D$.
2. Time periods in which no distance measurement is available at all (red area in Fig. 5). Additionally, periods of up to multiple measurement epochs occur in a recurring manner, while the electronic distance measurement (EDM) unit is recalibrating during tracking mode. In addition, it might be legit to use angle-only tracking mode in some applications.

The visualized simulation run is simulated similar to Fig. 2 with an additional static time window of 5 s at the end but with horizontal directions R of about 50 gon because in this scenario, we want to have equal contributions of Δ_D to x- and y-components. If we analyze the individual test quantities in the first row of Fig. 5, we can see that distance outliers Δ_D can be localized using test statistic (19) when using the spherical measurement model (left). In contrast, when using the cartesian measurement model, a smearing effect is visible, meaning that the outlier is split between the two horizontal components. For the same reason, one can see in the true errors (second row) that the cartesian model is subject to a bias (gray areas and chronologically following). This results from the fact that distance errors cannot be detected at all or parts of it cannot be detected.

For the red area, where no distance measurement is available for 1 s, the cartesian measurement model (right) is not able to provide any measurement update information. Therefore, both bias and estimated SD increase as the filtering solution relies solely on inertial navigation. Unsupported inertial navigation is prone to accumulated white noise of the IMU sensors. In contrast, the spherical model is supported in at least two directions (orthogonal to the line of sight), since it is possible to use angle measurements R and ζ. For this specific case of horizontal LOS, we can see that the height component accuracy does not suffer from missing distance measurements, as shon in the bottom row of Fig. 5.

Both effects, outlier detection and support of inertial navigation strongly depend on the measured horizontal direction R, as shown in Fig. 6. Again, the following considerations apply to approximately horizontal arrangement of RTS and prism. In measurement configurations where $R \approx 100gon$ or $R \approx 300gon$ a distance outlier mainly corrupts the y-component and for directions $R \approx 200gon$ or $R \approx 0gon/400gon$ it mainly corrupts the x-component. In these cases, where the target (prism) point is close to one of the coordinate axes the failure identification and elimination capabilities of the spherical measurement model are identical to those of the cartesian measurement model, compare the blue areas in Fig. 6. Outliers are detected at the corresponding tests of coordinate components using the cartesian measurement model.

The further away the target point is from the coordinate axes (horizontal directions of 50, 150, 250, 350 gon), the more significant the advantage of the spherical observation

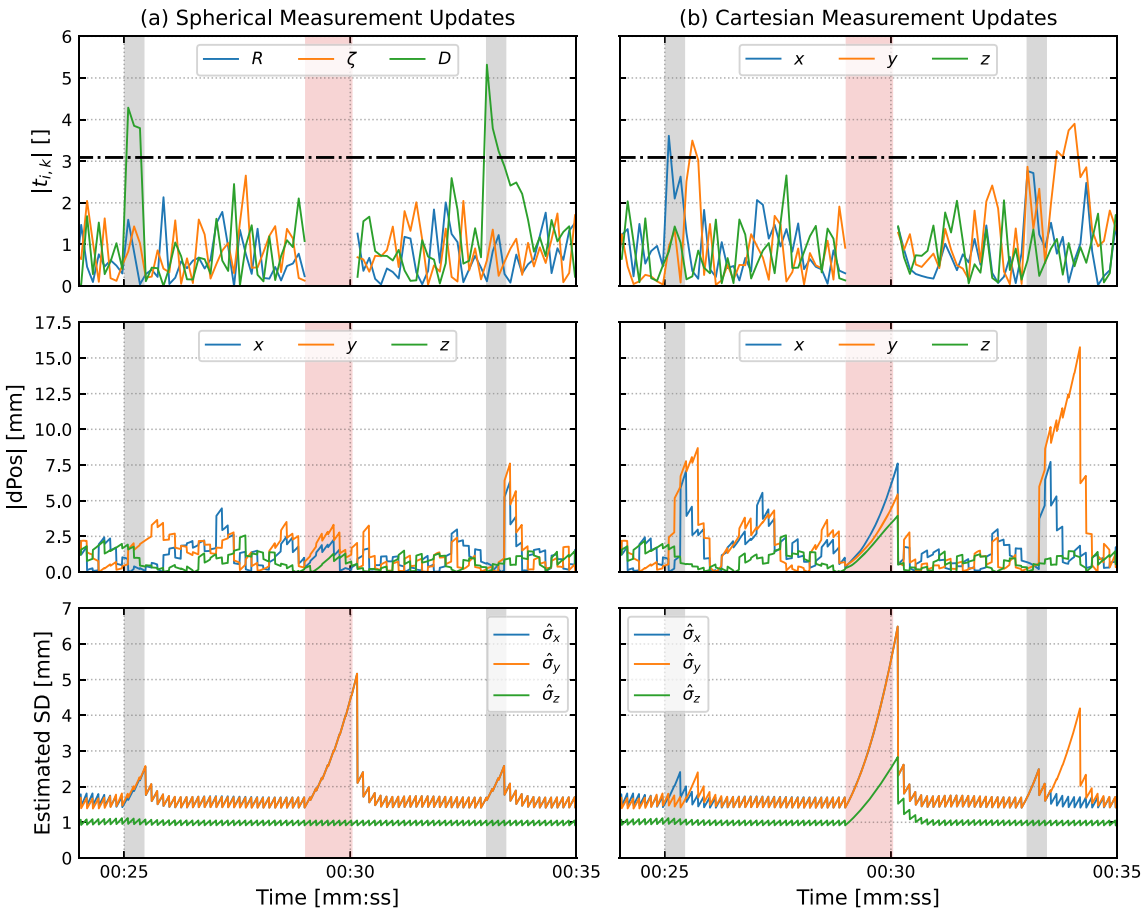

Fig. 5 Test statistics, true error for estimated position (dPos) and estimated standard deviation (SD) for **(a)** spherical measurement updates **(left)** and **(b)** cartesian measurement updates **(right)**. Gray areas indicate 0.45 s windows of distance outliers of MDB magnitude (14.3 mm). The red area indicates a distance outage of 1 s duration

model becomes. In Fig. 6, the red area indicates those constellations in which an outlier in the distance measurement cannot be detected in either one of the horizontal components of the cartesian measurement model. Whereas the identification capabilities of the spherical measurement model is independent of the horizontal direction R, compare the blue line in Fig. 6.

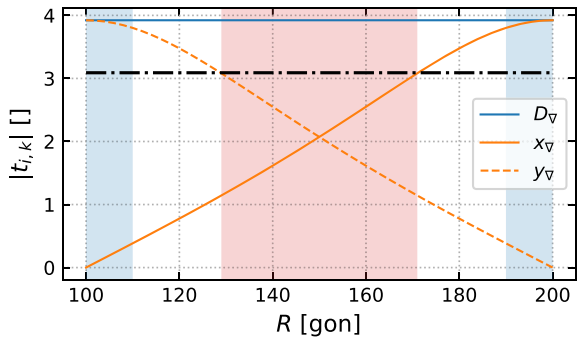

Fig. 6 Cartesian test statistics for x and y and spherical test statistic D for a distance bias of MDB magnitude over different horizontal directions R. The black line indicates the $1 - \alpha_q/2$ standard normal distribution percentile identifying the decision threshold ($z_{1-\alpha_q/2}$)

To conclude the investigations on measurement models and failure identification over the whole range of $R = 0gon$ to $R = 400gon$: For the second quadrant shown in Fig. 6 there are regions (blue) where both models are nearly identical (100 to 110 gon and 190 to 200 gon), which is 20%. From 130 to 170 gon (which is 40%, red area) the cartesian model is crucially malfunctioning and in the white areas in between (40%) the spherical measurement model is beneficial over the cartesian model. As this situation is similar in all other quadrants this gives an area of 80 gon for equal performance, 160 gon of worse identifiability and 160 gon of failure for the cartesian measurement model.

Smart pole experiments

To validate the developed methods and approaches in a practical application, we chose tilt compensation for an RTS pole. Such a setup is very similar to a probing device used in indus-

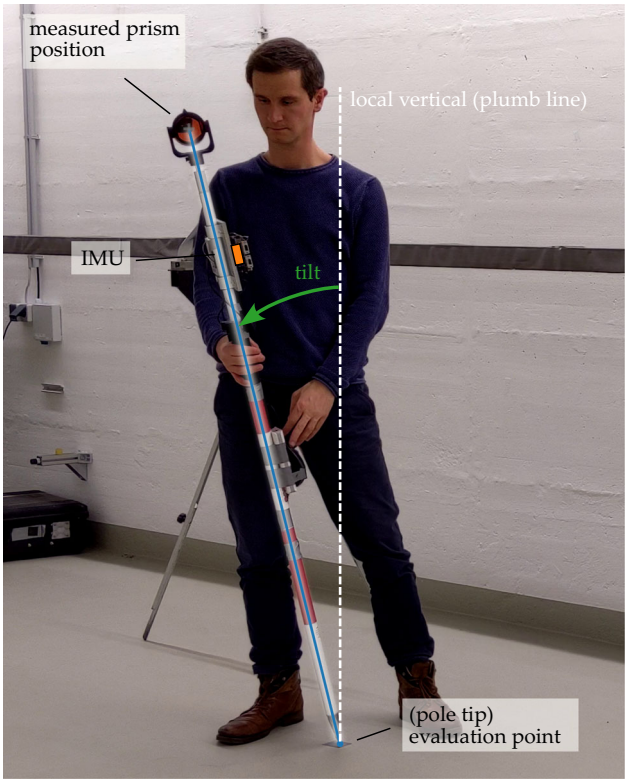

Fig. 7 Illustration of smart pole for RTS evaluation experiment. The pole tip is located at the reference evaluation point. As an example of RTS/INS fusion, the location of the pole tip is located by fusion of the measured prism position and INS data. The deviation of the pole from the plumb line is treated as the tilt angle

trial metrology. Compared to a laser scanning system, the determination accuracy of specific reference points can be eliminated, which allows better conclusions about the 6DoF accuracy.

With relatively low velocities (max. 1.6m/s), low external influences such as vibrations, a small distance between RTS and prism/system and a small distance between system and object point of interest (pole tip with a length of 1.6 m), such a setup can be seen as a preliminary study for 6DoF trajectory estimation of UAV (Unmanned Areal Vehicle) or UGV (Unmanned Ground Vehicle) mounted MMSs or any other robotic applications.

The downside of this test setup is that the distance measurement provides consistently reliable data, or the testing strategy does not indicate an outlier. On the one hand, this has to do with the low velocity of the prism and on the other hand with the relatively high MDB of 14.3 mm mentioned above.

Prerequisites

The methodology for tip point computation (also ground point computation or tilt compensation) was presented in Luo et al. (2018) for GNSS and in Thalmann et al. (2020) for RTS. It involves 6DoF trajectory estimation by a tight coupling RTS/INS fusion in an EKF framework as described in "Methodology". Since RTS measures position of the prism and the position of the pole tip is of interest, both positions need to be known w.r.t. to the INS. These vectors are called leverarm (prism) and tipvector (pole tip) and are determined using a lasertracker in the laboratory w.r.t. a pole-frame. The additional mounting rotation between this pole-frame and the INS needs to be determined. Our approach is described in Thalmann et al. (2020) and estimates mounting parameters with an accuracy of about 15 mgon. Please refer to Appendix C for more details on terminology and notation.

Time synchronization between RTS and IMU is solved using a wireless approach elaborating Network Time Protocol (NTP) over Wifi (cf. Thalmann and Neuner 2018) and a temporal calibration of RTS for kinematic applications estimating system latency, see Thalmann and Neuner (2021) for details on this approach. The achievable overall synchronization accuracy is specified by 0.2 ms.

The prototype of a tilt compensating pole consists of a MEMS IMU (Xsens MTi-600 series) and a Raspberry Pi 3 serving as a data collection and synchronization unit supplying a button to trigger point (static) or path (kinematic) measurement. The RTS is of type Leica TS16 and is also controlled by a Raspberry Pi 3, and a standard 360°-prism is mounted on the pole. The pole length of the prototype is 1.60 m with the IMU sitting 0.30 m below the prism. The data

Table 2 Smart pole evaluation results

Experiment	x_{RMSE}	y_{RMSE}	z_{RMSE}	$\sigma_{H,2D}$	$\sigma_{H,3D}$
Static 1 ($n = 63$) *(tilt = 15.5* gon *avg.)*	4.7	4.8	3.3	6.8	7.5
Static 2 ($n = 49$) *(tilt = 6.3* gon *avg.)*	1.8	1.7	1.3	2.5	2.8
Static 3 ($n = 58$) *(tilt = 8.8* gon *avg.)*	4.7	3.7	3.3	5.7	7.1
Kinematic 1 ($v = 0.7$m/s $avg.$; $tilt = 10.3$ gon $avg.$)	12.9	14.5	6.4	19.4	20.4
Kinematic 2 ($v = 0.6$m/s $avg.$; $tilt = 11.9$ gon $avg.$)	14.0	10.2	4.6	17.3	17.9
Kinematic 3 ($v = 0.5$m/s $avg.$; $tilt = 9.9$ gon $avg.$)	11.9	9.2	3.2	15.0	15.3

All units are [mm]

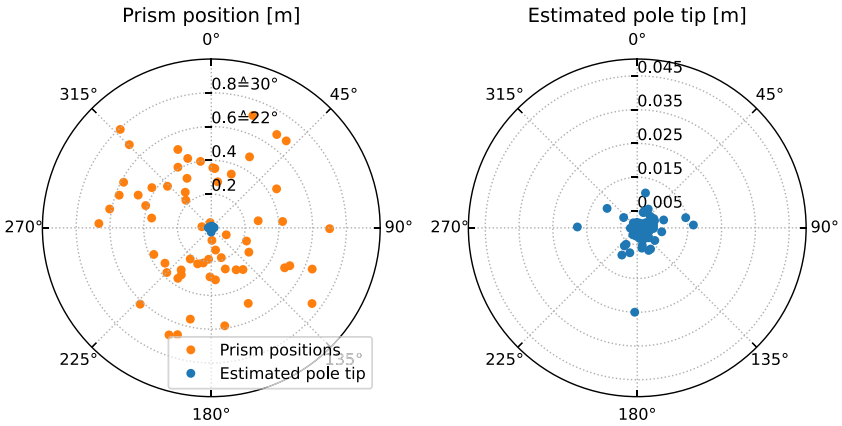

Fig. 8 Evaluation experiment static 1 ($n = 63$). **(left)** Prism positions w.r.t to the displacement from the plumbline (of the respective evaluation points) and the angle of displacement. **(right)** Tilt compensated deviations of the pole tip (the measured evaluation point) from ground truth values

collection is based on the popular Robotic Operating System (ROS) Framework which allows modularity and interoperability for future prototypes. For more details on ROS, see Linzer et al. (2022).

Evaluation

Evaluation experiments are carried out in the measurement laboratory utilizing five evaluation points marked on the floor. These evaluation points are stabilized reference points for the pole tip and their coordinates are determined with a lasertracker for ground truth.

A total of 3 measurement campaigns are carried out. Each one starts with an initialization routine similar to the one described in "Simulation studies" at one evaluation point. After that, each campaign contains two experiments. The first imitates static single point measurements, where the evaluation points are measured at a random pole tilt (angle between pole and plumb line), respectively prism position. Each point measurement is held static for approximately 1 s intervals by hand. This process is illustrated in Fig. 7. Subsequently, a kinematic experiment is performed where the tip stays fixed at an evaluation point and the prism is moved by circular and linear movements of different velocities.

A summary of the RMSE (root-mean-square error) values after tilt compensation is shown in Table 2. Exemplary prism positions (left) and errors for the estimated tip point w.r.t to ground truth evaluation points (right) of static experiment 1 are shown in Fig. 8.

For both static and kinematic experiments we can see, that the z-coordinate (height component) shows the lowest RMSE. Additionally, the x- and y-coordinates are more or less equal. This is exptectable since the working area is perfectly horizontal and the evaluation points are distributed in such a way that both x- and y-coordinates are similarly influenced by the RTS distance measurement (D). For the static experiments, a correlation between tilt and 2D Helmert point accuracy (2D RMSE[2], $\sigma_{H,2D} = \sqrt{x_{RMSE}^2 + y_{RMSE}^2}$) can be assumed. We have analyzed this tilt dependency, which is shown in Fig. 9.

The linear model (*Static Tilt*) indicates an accuracy of 2.0 mm + 0.2 mm per gon tilt. However the majority of the 170 measured single points were tilted below 15 gon, because for higher tilts, it is difficult for the operator to keep the pole tip centered at the evaluation point. The validity of this model for higher tilts must be further investigated. For comparison, the conventional method of single point measurement with a pole leveled by a standard 8′ circular level gives a standard deviation of approximately 2.6 mm. This value is composed of 1.3 mm accuracy of the circular level at a pole length of 1.6

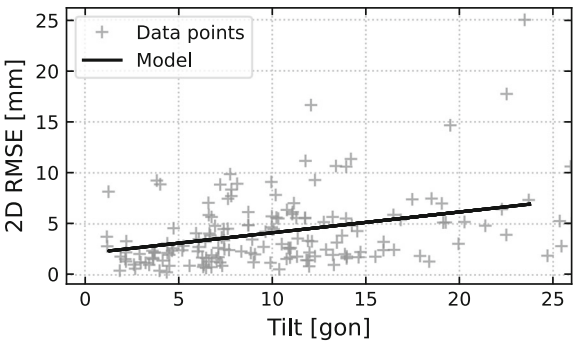

Fig. 9 Static evaluation point (=pole tip) error statistics dependent on tilt magnitude. The black line shows a linear model for 2D RMSE ($\sigma_{H,2D}$) estimated over all 170 data points

[2] For unbiased data of sufficient length RMSE and SD are interchangable because the different normalization (SD: $1 - n$, RMSE: n) has no significant effect.

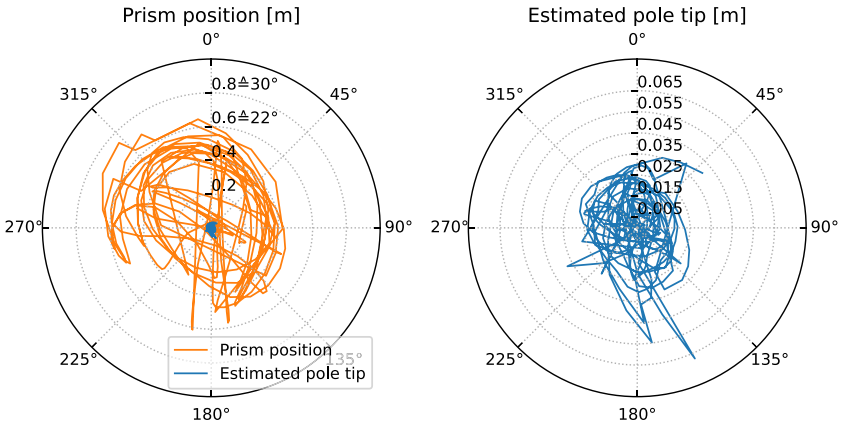

Fig. 10 Evaluation experiment kinematic 2 ($v = 0.6m/s$). **(left)** Prism positions w.r.t to the displacement from the plumbline (of the respective evaluation point) and the angle of displacement. **(right)** Tilt compensated deviations of the pole tip (the measured evaluation point) from ground truth values

m, 1.0 mm ATR/Angle accuracy, and 2.0 mm EDM accuracy ($\sqrt{1.0^2 + 1.3^2 + 2.0^2}$). We can conclude that our approach for static tilt compensation shows comparable accuracy at low tilts compared to conventional methods using a circular level.

As mentioned before these experiments are meant to be a preliminary study for kinematic 6DoF systems.Therefore, we do not limit our investigations to static applications. An example dataset of a kinematic experiment is shown in Fig. 10. From Table 2 we can deduce an influence of the moving speed of the prism on the expected accuracy of the pole tip. In addition, a tilt dependence is also expected in the kinematic case. Both dependencies (*Kinematic Tilt* and *Kinematic Velocity*) are shown in Fig. 11.

The data points over all three kinematic experiments are within 1.6 gon and 24 gon tilt (see Fig. 11(a)) and below 1.6 m/s (see Fig. 11(b)). The increase in standard deviation over the data range is more evident for tilt than for velocity. The reason for the tilt dependency of 0.8 mm per gon tilt might be the accuracy of the yaw angle estimation, which is usually 9 times worse than roll and pitch angles. The last two are stabilized by sensing gravity, whereas yaw depends on horizontal acceleration changes. The reason for the increasing standard deviation with higher velocity might be twofold. First, the pole tip slightly slides back and forth on the stabilization of the evaluation point at higher velocities in combination with tilts. Second, the noise of the clock readings (if the timestamp is interpreted as a time observing sensor) contributes a part of the overall noise and this proportion increases with higher velocity.

A combined kinematic stochastic model for pole tilt compensation (for a pole length of 1.60 m) indicates a base 2D RMSE of 3.8 mm for almost static and almost vertical poles, increasing by 6 mm for 10 gon tilt and 4.8 mm for velocities of 1 m/s. The evaluation results are summarized in Table 3.

Conclusion

Based on the research conducted on the sensor fusion of Robotic Total Station and Inertial Navigation System for 6DoF pose estimation, it can be concluded that the integration of these two sensors has the potential to improve accuracy and precision and unlock a broad range of applications.

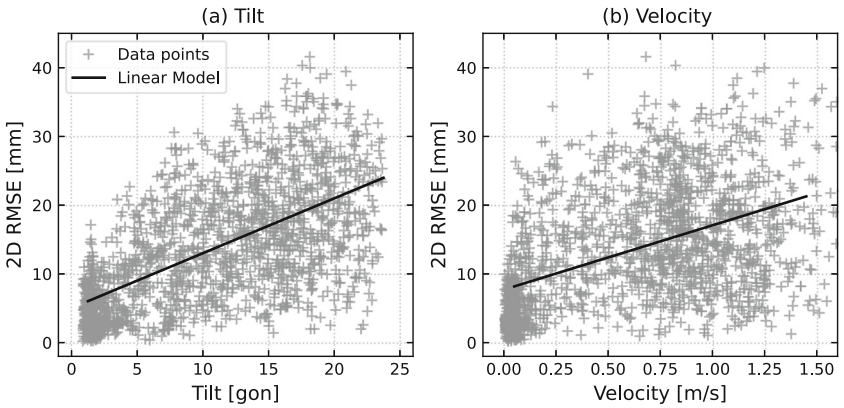

Fig. 11 Ground point 2D RMSE for kinematic experiments depends on **(left, a)** tilt and **(right, b)** velocity. The black lines show linear models of $\hat{\sigma}_{H,2D}$ estimated over all data points

Table 3 Pole tip accuracy models (in terms of 2D-RMSE, $\sigma_{H,2D}$) for a pole length of 1.6 m

Model	2D RMSE	
Conventional	approx. 2.6 mm	not applicable
Static Tilt	2.0 mm	+ 0.2 mm per gon Tilt
Kinematic Tilt	5.0 mm	+ 0.8 mm per gon Tilt
Kinematic Velocity	7.7 mm	+ 9.4 mm per m/s Velocity
Kinematic	3.8 mm	+ 0.6 mm per gon Tilt + 4.8 mm per m/s Velocity

The development of a novel measurement model for Robotic Total Station spherical measurements introduces tight coupling for RTS/INS sensor fusion. This approach provides significant advantages in supporting INS in cases where no distance measurements are available and performing outlier detection in epochs where distance measurement accuracy cannot be guaranteed. However, it is important to note that this model has two drawbacks, namely, computational complexity and potentially increased nonlinearity compared to the cartesian 3D position model.

Simulation studies are conducted to evaluate the derived approach. These studies have shown that a replacement of GNSS with RTS is advantageous even with high-end receivers in GNSS-ideal environments. The improvement ranges from 7% to 55% in position and attitude estimation. With the help of this simulation environment, we also show that a cartesian 3D position model can cause severe KF problems in 40% of the application range if the original raw spherical measurements are prone to distance outliers. With our tightly coupled RTS/INS approach we are able to identify and eliminate such failures.

In conclusion, the practical application of the developed methods and approaches for tilt compensation of the RTS pole provided valuable insights into the accuracy and precision of a prototype system. For kinematic applications of up to 1.5 m/s the stochastic model for the tilt compensated tip point indicated a base 2D-RMSE of 3.8 mm for almost static and almost vertical poles, increasing by 6 mm for 10 gon tilt and 4.8 mm for velocities of 1 m/s.

These results demonstrate the effectiveness of the developed methods and approaches for tilt compensation of the RTS pole, which can lead to improved accuracy and reliability in 6DoF pose estimation. Further research in this area can lead to the development of more advanced and precise kinematic measurement systems for surveying, construction, and robotics applications.

Appendix A Kalman filter notations

Our approach is based on a linearized discrete-time Kalman filter. The Error State formulation for RTS/INS fusion system and measurement models are:

$$\begin{aligned} \delta \boldsymbol{x}_k &= \boldsymbol{T}_{k-1,k}\, \delta \boldsymbol{x}_{k-1} + \boldsymbol{w}_k \\ \delta z_k &= \boldsymbol{H}_k\, \delta \boldsymbol{x}_k + \boldsymbol{v}_k \end{aligned} \tag{A1}$$

with

$$\begin{aligned} \boldsymbol{w}_k &\sim \mathcal{N}\left(0,\, \boldsymbol{Q}_k\right) \\ \boldsymbol{v}_k &\sim \mathcal{N}\left(0,\, \boldsymbol{R}_k\right) \\ \boldsymbol{w}_k &\quad \text{...System noise at epoch } k \\ \boldsymbol{Q}_k &\quad \text{...Variance Covariance Matrix (VCM) of system noise at epoch } k \\ \boldsymbol{v}_k &\quad \text{...Measurement noise at epoch } k \\ \boldsymbol{R}_k &\quad \text{...VCM of measurement noise at epoch } k \end{aligned} \tag{A2}$$

Prediction and Update Steps are:

$$\begin{aligned} \delta \bar{\boldsymbol{x}}_k &= \boldsymbol{T}_{k-1,k}\, \delta \hat{\boldsymbol{x}}_{k-1} \\ \bar{\boldsymbol{P}}_k &= \boldsymbol{T}_{k-1,k}\, \hat{\boldsymbol{P}}_{k-1}\, \boldsymbol{T}_{k-1,k}^T + \boldsymbol{Q}_{k-1} \\ \boldsymbol{d}_k &= \delta z_k - \boldsymbol{H}_k\, \delta \bar{\boldsymbol{x}}_k \\ \boldsymbol{D}_k &= \boldsymbol{R}_k + \boldsymbol{H}_k\, \bar{\boldsymbol{P}}_k\, \boldsymbol{H}_k^T \\ \boldsymbol{K}_k &= \bar{\boldsymbol{P}}_k\, \boldsymbol{H}_k^T\, \boldsymbol{D}_k^{-1} \\ \delta \hat{\boldsymbol{x}}_k &= \delta \bar{\boldsymbol{x}}_k + \boldsymbol{K}_k\, \boldsymbol{d}_k \\ \hat{\boldsymbol{P}}_k &= (\boldsymbol{I} - \boldsymbol{K}_k\, \boldsymbol{H}_k)\ \bar{\boldsymbol{P}}_k \end{aligned} \tag{A3}$$

where

$\delta\bar{\boldsymbol{x}}_k$ ...Predicted error state at epoch k
$\bar{\boldsymbol{P}}_k$ ...VCM of predicted (error) state vector at epoch k
$\boldsymbol{d}_k$ ...Vector of innovations at epoch k
$\boldsymbol{D}_k$ ...VCM of innovations
$\boldsymbol{K}_k$ ...Kalman gain matrix

$\delta\hat{\boldsymbol{x}}_k$ ...Estimated error state at epoch k
$\hat{\boldsymbol{P}}_k$ ...VCM of estimated (error) state vector at epoch k (A4)

Appendix B Mean shift model and test quantity derivation

Our testing strategy is based on the mean shift model applied to the Gauss-Markov representation of the filter update:

$$\begin{bmatrix}\delta\boldsymbol{z}_k\\ \delta\bar{\boldsymbol{x}}_k\end{bmatrix}=\begin{bmatrix}\boldsymbol{H}_k & \boldsymbol{E}\\ \boldsymbol{I} & \boldsymbol{0}\end{bmatrix}\begin{bmatrix}\delta\boldsymbol{x}_k\\ \boldsymbol{\Delta}\end{bmatrix}+\begin{bmatrix}\boldsymbol{d}_k\\ \boldsymbol{w}_k\end{bmatrix} \tag{B5}$$

where $\boldsymbol{\Delta}$ describes the modeled bias vector of dimension q. Matrix $\boldsymbol{E}$ describes the influence of the bias on the measurements. With $\boldsymbol{\Delta}$ and $\boldsymbol{E}$, we are able to model and test against different error scenarios, e.g., in this publication a group of outliers (B13) or a bias from a different observation space (B14). Matrix $\boldsymbol{E}$ can be found by modeling

$$z_k^{\Delta}=\boldsymbol{E}\ \boldsymbol{\Delta} \tag{B6}$$

implying the dimensions of $\boldsymbol{E}$ of the number of observations (n_k) times the number of modeled outliers (q).

Test quantity $T_{\boldsymbol{\Delta}}$ for the hypotheses H_0 and H_a is well known, cf. Teunissen (2006, p. 72ff):

$$\begin{aligned}&H_0: E\{\boldsymbol{\Delta}\}=\boldsymbol{0}\\ &H_a: E\{\boldsymbol{\Delta}\}\neq\boldsymbol{0}\\ &T_{\boldsymbol{\Delta}}=\hat{\boldsymbol{\Delta}}^T\ \boldsymbol{\Sigma}_{\hat{\boldsymbol{\Delta}}}^{-1}\ \hat{\boldsymbol{\Delta}}\end{aligned} \tag{B7}$$

and follows a $\chi^2_{1-\alpha_q,q}$ distribution. The estimated bias vector and the corresponding VCM are computed by (cf. Jäger et al. 2005, p. 184ff):

$$\begin{aligned}\hat{\boldsymbol{\Delta}}&=\boldsymbol{\Sigma}_{\hat{\boldsymbol{\Delta}}}\boldsymbol{E}^T\boldsymbol{D}_k^{-1}\boldsymbol{d}_k\\ \boldsymbol{\Sigma}_{\hat{\boldsymbol{\Delta}}}&=\left(\boldsymbol{E}^T\boldsymbol{D}_k^{-1}\boldsymbol{E}\right)^{-1}\end{aligned} \tag{B8}$$

Inserting (B8) into (B7) gives

$$\begin{aligned}T_{\boldsymbol{\Delta}}&=\boldsymbol{d}_k^T\boldsymbol{D}_k^{-1}\boldsymbol{E}\ \left(\boldsymbol{E}^T\boldsymbol{D}_k^{-1}\boldsymbol{E}\right)^{-1}\overbrace{\left(\boldsymbol{E}^T\boldsymbol{D}_k^{-1}\boldsymbol{E}\right)\left(\boldsymbol{E}^T\boldsymbol{D}_k^{-1}\boldsymbol{E}\right)^{-1}}^{=\boldsymbol{I}}\boldsymbol{E}^T\boldsymbol{D}_k^{-1}\boldsymbol{d}_k\\ &=\boldsymbol{d}_k^T\boldsymbol{D}_k^{-1}\boldsymbol{E}\ \left(\boldsymbol{E}^T\boldsymbol{D}_k^{-1}\boldsymbol{E}\right)^{-1}\ \boldsymbol{E}^T\boldsymbol{D}_k^{-1}\boldsymbol{d}_k\quad .\end{aligned} \tag{B9}$$

For an individual outlier $q=1$ with $\boldsymbol{E}=\boldsymbol{\eta_i}$ (being the i-th canonical unit vector) expression (B9) can be further simplified because

$$\boldsymbol{E}^T\boldsymbol{D}_k^{-1}\boldsymbol{E}=\boldsymbol{\eta}_i^T\boldsymbol{D}_k^{-1}\boldsymbol{\eta}_i=\sigma_{d_i}^2 \tag{B10}$$

is the variance of the i-th innovation. This gives

$$\begin{aligned}T_{i,k}&=\boldsymbol{d}_k^T\boldsymbol{D}_k^{-1}\boldsymbol{\eta}_i\ \frac{1}{\sigma_{d_i}^2}\ \boldsymbol{\eta}_i^T\boldsymbol{D}_k^{-1}\boldsymbol{d}_k=\\ &=\frac{1}{\sigma_{d_i}^2}\ \left(\boldsymbol{\eta}_i^T\boldsymbol{D}_k^{-1}\boldsymbol{d}_k\right)^T\ \left(\boldsymbol{\eta}_i^T\boldsymbol{D}_k^{-1}\boldsymbol{d}_k\right)=\\ &=\frac{\left(\boldsymbol{\eta}_i^T\boldsymbol{D}_k^{-1}\boldsymbol{d}_k\right)^2}{\sigma_{d_i}^2}\end{aligned} \tag{B11}$$

Taking the square root $t_{i,k}=\sqrt{T_{i,k}}$ and resubstituting (B10) gives (19). The test quantity $|t_{i,k}|$ follows a standard normal distribution $z_{1-\alpha_q/2}$ because $\sqrt{T_{i,k}}\sim\chi_{1-\alpha_q,1}$ and from $X\sim\chi_1$ follows $|X|\sim z$ (standard normal distribution).

B.1 Group of measurements

Two strategies to overcome identifyability issues with the cartesian measurement model are possible. The first is to test two components at a time, e.g., the x- and y-components for a vertical angle ζ of approximately 100 gon.

With $q=2$, we model a two-dimensional bias vector, e.g., $\boldsymbol{\Delta}_{xy}=\left[\Delta_x\ \Delta_y\right]^T$. The test then yields:

$$\begin{aligned}&H_{a,I,k}: E\{\delta\boldsymbol{z}_k\}=\boldsymbol{H}_k\delta\boldsymbol{x}_k+\boldsymbol{E}\boldsymbol{\Delta}\\ &T_{I,k}=\boldsymbol{d}_k^T\boldsymbol{D}_k^{-1}\boldsymbol{E}\left(\boldsymbol{E}^T\boldsymbol{D}_k^{-1}\boldsymbol{E}\right)^{-1}\boldsymbol{E}^T\boldsymbol{D}_k^{-1}\boldsymbol{d}_k\\ &T_{I,k}>\chi^2_{1-\alpha_q,q}\end{aligned} \tag{B12}$$

with

$$\boldsymbol{E} = \begin{bmatrix} 1 & 0 \\ 0 & 1 \\ 0 & 0 \end{bmatrix} \tag{B13}$$

B.2 Cartesian distance bias

The other approach is to model a distance measurement outlier $\Delta = \Delta_D$ for the cartesian measurement model. this leads to the same test statistic (B12) with

$$\boldsymbol{E} = \begin{bmatrix} \sin\zeta_{la}^{l} & \cos R_{la}^{l} \\ \sin\zeta_{la}^{l} & \sin R_{la}^{l} \\ -\cos\zeta_{la}^{l} & \end{bmatrix} \tag{B14}$$

and $q = 1$.

B.3 Comparison

The two alternate testing strategies for the cartesian model are shown in Fig. 12 together with the test quantity of the distance measurement for the spherical model. It represents the same simulated data as Fig. 5. The test quantity $T_{D,k}$ is slightly different from Fig. 5 because measurement elimination is disabled for better comparison with the cartesian testing strategies.

We can see that the xy-group test ($T_{xy,k}$, dashed line, Eq. B13) is slightly disadvantageous compared to the test statistic for the spherical distance measurement ($T_{D,k} = t_{D,k}^2$, dotted line, Eq. 19). On the other hand, the test statistic for cartesian formulated distance bias ($T_{D_c,k}$, solid line, Eq. B14) is identical to the corresponding spherical statistic in terms of identifiability. However, the problem with this cartesian test strategy is that the possibility of elimination is missing after failure identification. At the latest when the null hypothesis has to be rejected, the spherical observation model is necessary to be able to eliminate the faulty observation.

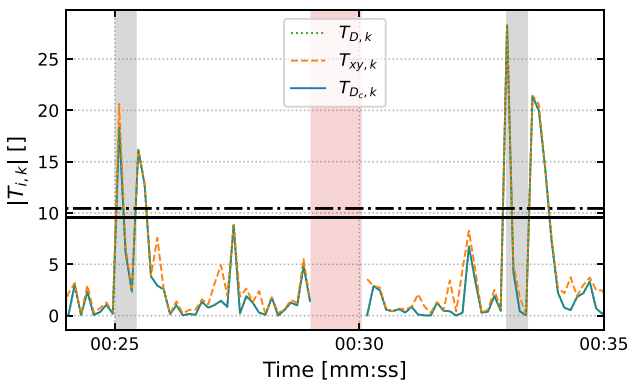

Fig. 12 Test statistics for individual distance measurement in the spherical model compared to the xy-group test $T_{xy,k}$ (B13) and the distance bias for cartesian measurement model $T_{D_c,k}$ (B14). The solid black line is the threshold for an individual test, the dashed line is the corresponding threshold for the group test

Appendix C Pole tilt compensation methodology

Pole tilt compensation describes the process of computationally leveling a tilted pole or probing device to measure the coordinates of the tip. This boils down to a series of coordinate transformations.

First, we have the pole system p-frame, which is defined in terms of a right-handed coordinate system with the origin at the prism center and the z-axis through the pole tip. In this system, we measure the tip (subscript $_v$), prism center ($_a$) and IMU position ($_b$) with a higher-order accuracy system, e.g., a lasertracker. From this we are able to compute the prism-tip-vector $\boldsymbol{l}_{av}^{p}$, the imu-tip-vector $\boldsymbol{l}_{bv}^{p}$ and the imu-prism-vector $\boldsymbol{l}_{ba}^{p}$ using the above specified subscripts. These have to fulfill the following condition by definition (with l_p describing the pole length between prism center and pole tip):

$$\boldsymbol{l}_{av}^{p} = \boldsymbol{l}_{bv}^{p} - \boldsymbol{l}_{ba}^{p} = \begin{bmatrix} 0 \\ 0 \\ l_p \end{bmatrix} \tag{C15}$$

The involved frames and vectors are shown in Fig 13. The imu-prism-vector $\boldsymbol{l}_{ba}^{p}$ w.r.t. the *body frame* (b-frame, respec-

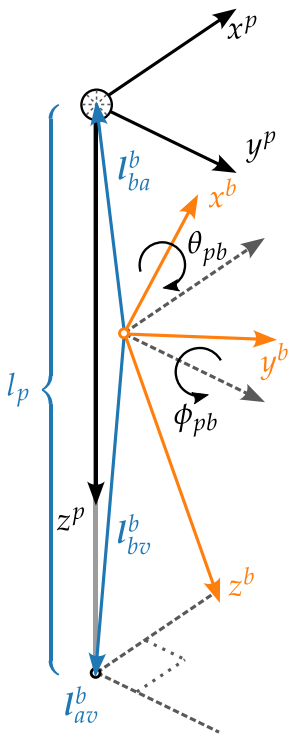

Fig. 13 The IMU body frame and the pole frame related by the mounting parameters $\boldsymbol{C}_p^b$. The relation between prism-tip-vector, imu-tip-vector (tipvector $\boldsymbol{l}_{bv}^b = \boldsymbol{C}_p^b\, \boldsymbol{l}_{bv}^p$) and imu-prism-vector (leverarm $\boldsymbol{l}_{ba}^b = \boldsymbol{C}_p^b\, \boldsymbol{l}_{ba}^p$) is shown in blue

tively the IMU) $\boldsymbol{l}^b_{ba} = \boldsymbol{C}^b_p \, \boldsymbol{l}^p_{ba}$ is called *leverarm* (or *mounting vector* in some references) and is needed in tight coupling of RTS/INS. We call the rotation between pole- and body frame $\boldsymbol{C}^b_p$ *mounting*, which describes the relation between the p-frame and b-frame and is caused by the mounting of the IMU on the pole. This *mounting* is calibrated beforehand, for details see Thalmann et al. (2020).

From the tight coupling approach of RTS and INS we derive the position $\boldsymbol{r}^l_{lb}$ and orientation $\boldsymbol{\psi}^l_{lb}$ of the b-frame, w.r.t. the *local tangent-plane frame*, the l-frame. The compensation is achieved by computing the tip w.r.t to the RTS l-frame $\boldsymbol{r}^l_{lv}$:

$$\begin{aligned} \boldsymbol{r}^l_{lv} &= \boldsymbol{r}^l_{lb} + \boldsymbol{C}^l_b \, \boldsymbol{l}^b_{bv} \\ \boldsymbol{r}^l_{lv} &= \boldsymbol{r}^l_{lb} + \boldsymbol{C}^l_b \, \boldsymbol{C}^b_p \, \boldsymbol{l}^p_{bv} \end{aligned} \tag{C16}$$

where $\boldsymbol{C}^l_b$ is the rotation matrix defined by Euler angles $\boldsymbol{\psi}^l_{lb}$ estimated within the EKF. The *tipvector* $\boldsymbol{l}^b_{bv}$ is computed by rotating the imu-tip-vector (p-frame, $\boldsymbol{l}^p_{bv}$) by the mounting $\boldsymbol{C}^b_p$.

Funding Open access funding provided by TU Wien (TUW).

Declarations

Conflicts of Interest The authors have no conflict of interest to declare that are relevant to this article.

References

Baarda W (1968) A testing procedure for use in geodetic networks. Netherlands geodetic commission, New Series 2/5

Bauer P, Jost S, Lienhart W (2020) Beurteilung der eignung eines vr-systems als 3d-koordinatenmesssystem. In: 19. Internationaler Ingenieurvermessungskurs: IVK2020, pp 15–28 . Wichmann Verlag

Eder R (2022) Evaluierung der Einsatzfähigkeit einer neuartigen lotstocktechnologie. Masterthesis, Hochschule für technik und Wirtschaft Dresden

Gao Y, Lin J, Yang L, Muelaner J, Keogh P, Zhu J (2017) Integrated calibration of a 3d attitude sensor in large-scale metrology. Meas Sci Technol 28(7)

Grewal MS, Andrews AP (2014) Kalman filtering - theory and practice with MATLAB. John Wiley & Sons

Groves PD (2013) Principles of GNSS, inertial, and multisensor integrated navigation systems. Artech house, ???

He M, Zhu C, Huang Q, Ren B, Liu J (2020) A review of monocular visual odometry. Visual Computer 36(5):1053–1065. https://doi.org/10.1007/s00371-019-01714-6

Hesse C, Holste K, Neumann I, Esser R, Geist M (2021) 3D hydromapper-ein innovatives messsystem für die erfassung, prüfung und das management von Wasser-Infrastrukturbauwerken. ZfV-Zeitschrift für Geodäsie, geoinformation und landmanagement (4)

Hesse C, Vennegeerts H (2014) Referenzierung kinematischer laserscansysteme mit IMU und tachymeter. Schriftenreihe des DVW 75 (multi-sensor-systeme - Bewegte Zukunftsfelder), 159–173

Heunecke O, Strübing T (2018) Stop & go messsysteme zur Gleisabsteckung und Gleisabnahme. MST 2018 - Multisensortechnologie: low-cost sensoren im Verbund, DVW-Schriftenreihe, Band 92 (92):77–89

Jäger R, Müller T, Saler H (2005) Klassische und robuste ausgleichungsverfahren. Wichmann Verlag, Heidelberg, p 340

Jwo DJ, Cho TS (2010) Critical remarks on the linearised and extended Kalman filters with geodetic navigation examples. Measurement: J Int Measure Conf 43(9):1077–1089 https://doi.org/10.1016/j.measurement.2010.05.008

Keller F (2016) Entwicklung eines forschungsorientierten multi-sensorsystems zum kinematischen Laserscanning innerhalb von Gebäuden, Dissertation. PhD thesis, HCU Hamburg

Kyle S, Loser R (2003) Concepts and components of a novel 6dof tracking system for 3d metrology. In: Optical 3-D measurement techniques VI, vol 2, pp 55–62

Leica Geosystems (2016) Leica TS16 user manual. Technical report, leica geosystems, Heerbrugg, Switzerland. https://surveyequipment.com/assets/index/download/id/845/

Lerke O, Schwieger V (2021) Analysis of a kinematic real-time robotic total station network for robot control. J Appl Geodesy 15(3):169–188

Li B, Wang Y, Zhang Y, Zhao W, Ruan J, Li P (2020) GP-SLAM: laser-based SLAM approach based on regionalized Gaussian process map reconstruction. Auton Robot 44(6):947–967. https://doi.org/10.1007/s10514-020-09906-z

Linzer F, Barnefske E, Sternberg H (2019) Robot operating system zur Steuerung eines modularen mobile-mapping-systems -Aufbau. Validierung und Anwendungen. Allgemeinde Vermessungsnachricht 1–2:21–29

Linzer F, Schild N-M, Paffenholz J-A (2022) Ros im multisensorsystem - am beispiel von geodätischen anwendungen. Multisensortechnologie: Von (A)nwendungen bis (Z)ukunftstechnologien, DVW-Schriftenreihe, Band 103

Luo X, Schaufler S, Carrera M, Celebi I (2018) High-precision RTK positioning with calibration-free tilt compensation high-precision RTK positioning with calibration-free tilt compensation. In: FIG Congress 2018 - embracing our smart world where the continents connect

Maar H (2022) Automated pole functionalities for advancing productivity of total station workflows. In: FIG Congress 2022 volunteering for the future - geospatial excellence for a better living, Warsaw, Poland, p 15

Maxim A, Lerke O, Prado M, Dörstelmann M, Menges A, Schwieger V (2017) UAV guidance with robotic total station for architectural fabrication processes. Unmanned aerial vehicles 2017, DVW-Schriftenreihe, Band 86 (92):145–161

Santerre R (1991) Impact of gps satellite sky distribution. Manuscr Geodaet 16:28–53

Schestauer B-J, Wagner A, Wiedemann W, Wunderlich T (2017) Tachymetrisches 6 dof messverfahren. In: 18. Internationaler Ingenieurvermessungskurs: IVK2017, pp 213–220 . Wichmann Verlag

Sternberg H, Keller F, Willemsen T (2013) Precise indoor mapping as a basis for coarse indoor navigation. J Appl Geodesy 7(4):231–246. https://doi.org/10.1515/jag-2013-0015

Strübing T (2015) Kalibrierung und Auswertung von lasertriangulationsbasierten multisensorsystemen am Beispiel des Gleisvermessungssystems RACER II. PhD thesis, München, Univ. der Bundeswehr, Diss., 2015

Teodori G, Neuner H (2021) Analysis of the yaw observability in gnss-ins integration for uav pose estimation. In: Contributions to international conferences on engineering surveying, pp 259–269. Springer

Teunissen PJ (1998) Quality control and gps. In: GPS for Geodesy, pp 271–318. Springer, ???

Teunissen PJ (2006) Testing theory. VSSD Delft, ???

Thalmann T, Neuner H (2021) Temporal calibration and synchronization of robotic total stations for kinematic multi-sensor-systems. J Appl Geodesy 15(1):13–30

Thalmann T, Neuner H (2018) Evaluation of the network time protocol for synchronization of multi-sensor-systems. avn - Allgemeine Vermessungsnachrichten 125(6):163–174

Thalmann T, Zechner M, Neuner H (2020) Accelerometer triad calibration for pole tilt compensation using variance based sensitivity analysis. Sensors 20(5) https://doi.org/10.3390/s20051481

Titterton D, Weston JL (2004) Strapdown inertial navigation technology vol 17, 2nd editio edn. IET, ???

Vaidis M, Dubois W, Guénette A, Laconte J, Kubelka V, Pomerleau F (2022) Extrinsic calibration for highly accurate trajectories reconstruction. arXiv:2210.01048

Vaidis M, Giguère P, Pomerleau F, Kubelka V (2021) Accurate outdoor ground truth based on total stations. In: 2021 18th Conference on Robots and Vision (CRV), pp 1–8

Wieser, A., Petovello, M.G., Lachapelle, G., Group, N.P. (2004) Failure scenarios to be considered with kine- matic high precision relative GNSS positioning. Ion Gnss 2004:1448–1459

Zhou Z, Liu W, Wang Y, Yue Y, Zhang J (2022) An accurate calibration method of a combined measurement system for large-sized components. Measure Sci Technol